Camphorsulfonic-Salified Chitosan Allowing MACl-Free Stabilization of Pure FAPbI₃ α-Phase via Gravure Printing in Ambient Air

Nadir Vanni, Antonella Giuri, Mario Calora, Edoardo Podda, Anna Paola Caricato, Katia Sparnacci, Riikka Suhonen, Mari Ylikunnari, Amanda Covarelli, Luca Gregori, Filippo De Angelis, Gianluigi Marra, Paolo Biagini, Riccardo Po, and Aurora Rizzo*

Metal–halide perovskites have gained extreme interest in the photovoltaic field with formamidinium lead iodide (FAPbI₃) currently being one of the best-performing materials for single-junction solar cells. Despite the outstanding record efficiencies, there are still several major issues hindering the large-scale fabrication of perovskite solar cells. The vulnerability to environmental agents along with the need of controlled atmosphere and crystallization aids for the perovskite film deposition represents the major roadblocks. This is particularly true for FAPbI₃ for which the thermodynamically stable phase at room temperature is photovoltaically inactive δ-phase. To address those challenges, herein, a camphorsulfonic-salified chitosan is specifically designed with the aid of DTF calculations to strongly interact with the perovskite and, as a result, improve the morphology and optoelectronic quality of the FAPbI₃. Thanks to the numerous interactions and then the modulation of the solution viscosity, FAPbI₃ devices are fabricated by gravure printing deposition without either antisolvent bath or inclusion of methylammonium chloride (MACl) as additive. The gravure-printed devices with the chitosan feature an enhanced efficiency and stability in air, retaining 80% of the original efficiency after 1200 h in ambient air without any encapsulation.

1. Introduction

Perovskite solar cells (PSCs) have emerged in recent years as the protagonists of the photovoltaic scene, holding out the hope of replacing the already established silicon solar cells. The great success and interest are due to the impressive optical and electrical properties of the material, including a high optical absorption coefficient, high defect tolerance, tunable bandgap, and high carrier mobility.[1–4] While incredible progress has been made in terms of both the power conversion efficiency (PCE)[5] and device stability,[6] there are still many steps to be taken to ensure the future commercialization of this technology. Some of the issues that arise in the transition from laboratory scale to manufacturing are the almost mandatory control of the environmental conditions during deposition[7] and of the crystallization of the perovskite.[8,9] Typically, the device is fabricated

N. Vanni, M. Calora, A. P. Caricato
Dipartimento di Matematica e Fisica "E. De Giorgi"
Università del Salento
Campus Ecotekne, via Arnesano, 73100 Lecce, Italy

N. Vanni, A. Giuri, M. Calora, A. Rizzo
CNR NANOTEC – Istituto di Nanotecnologia
Consiglio Nazionale delle Ricerche
c/o Campus Ecotekne, 73100 Lecce, Italy
E-mail: aurora.rizzo@nanotec.cnr.it

E. Podda, K. Sparnacci
Dipartimento di Scienze ed Innovazione Tecnologica
Università degli Studi del Piemonte Orientale "A. Avogadro"
via Michel 11, 15121 Alessandria, Italy

K. Sparnacci
UdR Piemonte Orientale
INSTM
Alessandria, Italy

R. Suhonen, M. Ylikunnari
Printed Functional Solutions
VTT Technical Research Centre of Finland
Kaitoväylä 1, FIN-90571 Oulu, Finland

A. Covarelli, L. Gregori, F. De Angelis
Department of Chemistry, Biology and Biotechnology
University of Perugia and INSTM
06123 Perugia, Italy

F. De Angelis
Institute of Energy Science and Technology (SIEST)
Sung kyun kwan University SKKU
Suwon 440-746, Korea

G. Marra, P. Biagini, R. Po
Renewable, New Energy and Material Science Research Center
Istituto Guido Donegani
Eni S.p.A.
via Fauser 4, I-28100 Novara, Italy

in an N_2-filled glovebox or at least in a low-humidity environment, as oxygen and water are known to be damaging for the perovskite[10] and moreover, the crystallization process must be monitored to avoid a disordered self-assembly in the film.[11] This is usually achieved by the antisolvent dripping technique, which induces a rapid supersaturation of the perovskite precursors during the film formation and rapid solvent evaporation.[12] In particular, these problems become more relevant when moving from spin-coater deposition to upscalable deposition methods, via roll to roll (R2R) which would bring PSCs closer to the possibility of commercialization, allowing for an efficient, fast, and low-cost deposition on lightweight and flexible substrates, making the need to overcome these limits even more urgent. Although some options to replicate the antisolvent dripping on R2R techniques exist, such as antisolvent bathing[13] and nitrogen blowing,[14,15] these require additional costs and optimization making the complete elimination of the need highly desirable.

In this context, formamidinium lead iodide ($FAPbI_3$) perovskite is one of the most promising candidates for single-junction PSCs because of the ideal bandgap of 1.48 eV,[16] which is allowed to achieve the highest efficiency so far,[17] and it has also a superior thermal stability.[18] However, the deposition of $FAPbI_3$ in larger scale represents an additional challenge, since its cubic photoactive phase (α-phase) is thermodynamically stable at high temperatures and it degrades into the hexagonal nonphotoactive phase (δ-phase) at room temperature,[19] plus this degradation is boosted by exposure to oxygen and humidity.[20,21] While several methods exist to stabilize the α-phase at room temperature,[22] none are without compromise. One of the most popular stabilization strategies is compositional engineering[23] by adding different size cations like cesium (Cs) and effectively stabilizing the α-phase; however, the value of the bandgap is inevitably changed resulting a decreased efficiency of light harvesting. The other well-known strategy to stabilize the α-phase $FAPbI_3$ is the use of MA-based additives, in particular the volatile methylammonium chloride (MACl) which directly promotes the formation of the α-phase by inducing MA-rich nuclei and boosts the crystallization during annealing.[24,25] However, the presence of MACl can be a source of instability since its hygroscopic nature, especially in a high-humidity atmosphere, can facilitate the degradation to the δ-phase[26] and it has been seen that the residual chlorine left in the film is detrimental to the device performances.[27] Moreover, the presence of MA^+ combined with FA^+ in the precursor's solution can promote the formation of harmful adducts, causing the formation of several hexagonal polytypes[28,29] during deposition. These factors affect the reproducibility of the method, especially in larger-scale applications where larger volumes of solutions are used and the control of the relative humidity is more complex.
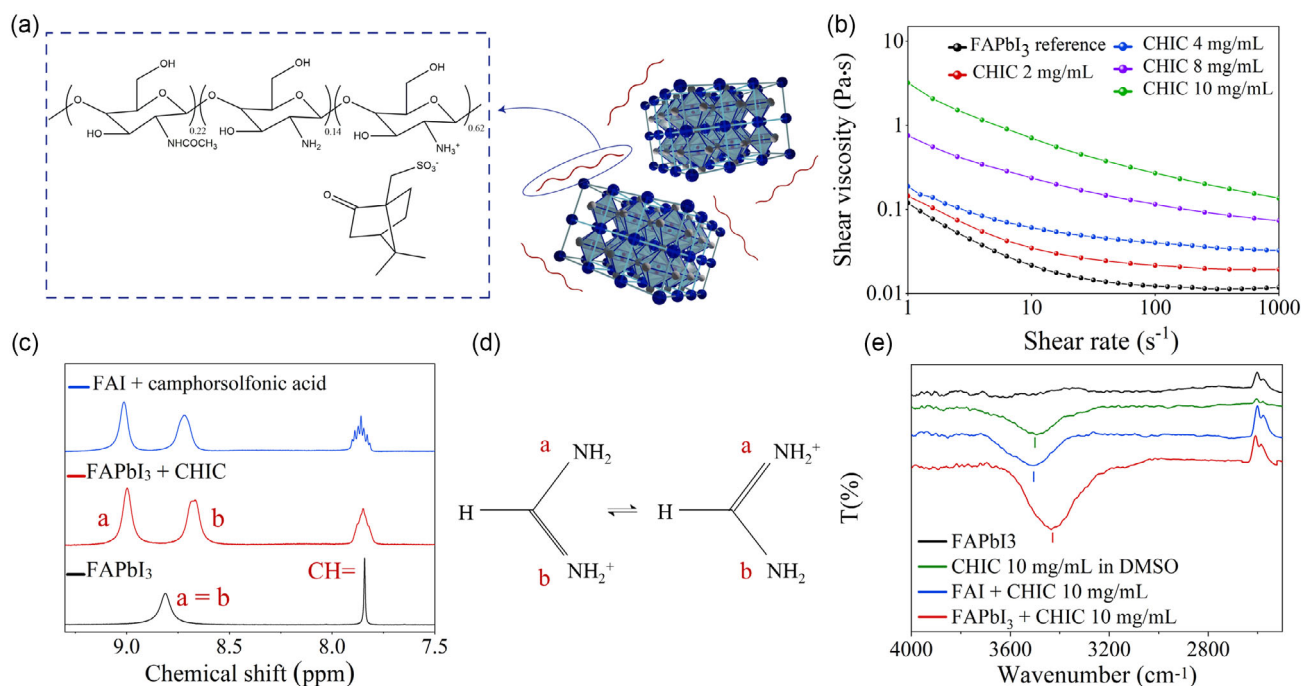
Herein, a camphorsulfonic-salified chitosan (CHIC) is proposed as an additive for $FAPbI_3$ to upscale the deposition of the perovskite by exploiting both the properties of this hydrophobic polymer and of the camphorsulfonic group added through the salification reaction, allowing us to not only obtain pure α-phase $FAPbI_3$ with superior morphology and fewer defects, but also to overcome the limitations of the environmental control and the antisolvent dripping. With this purpose, the present work is developed into two separate steps, first removing the N_2-controlled environment and operating in humid ambient air and next moving to the gravure printing deposition without the use of antisolvent. The role of the additive is elucidated by density functional theory (DFT) calculations and experimental data, confirming that in the system the perovskite interacts both with the chitosan and the camphorsulfonic group, resulting in numerous bonds which help in guiding the crystallization, thus making the use of antisolvent obsolete. Moreover, the chitosan modulates the viscosity of the solution, which is a critical parameter for the gravure technique as it allows to print a high-resolution pattern. The perovskite via gravure printing is tested in a direct n–i–p PSC, demonstrating the versatility and compatibility of the perovskite–polymer composite, which exhibits in both cases superior properties to the reference perovskite with higher photoluminescence (PL) lifetimes and better morphologies. In particular, it was found that adding the salified chitosan in the $FAPbI_3$ solution enabled the elimination of MACl as additive to promote the α-phase formation, effectively depositing the pure α-phase perovskite with the gravure printing deposition for the first time without any other additive or other crystallization aids such as the antisolvent bath.

2. Results and Discussion

Before incorporating the chitosan into the perovskite solution and taking advantage of the polymer's properties, a chemical modification was needed, both to ensure the solubility in the perovskite precursors' solution and, most importantly, to functionalize the structure in order to maximize the interaction with the perovskite. Camphorsulfonic acid was chosen for the salification of the aminic group of the chitosan for the interaction that the sulfonate group can establish with the perovskite, especially with the uncoordinated surface Pb^{2+} ions.[30–32] Following this procedure, which can be found in the Supporting Information, the resulting salified chitosan becomes soluble in dimethyl sulfoxide (DMSO) and it can be used as an additive into perovskite precursor inks (**Figure 1**a). Accordingly, DMSO was chosen as the sole solvent for our $FAPbI_3$ perovskite solution, which is conveniently a low-toxicity solvent[33] and therefore suitable for scalable techniques and air deposition. The salified polymer solubilized in the solvent causes a drastic modulation of the rheological behavior of the solution and the steady viscosity as a function of the shear rate is shown in Figure 1b. It is already established that several polymers can enhance the viscosity of solutions, and this property was already exploited in similar systems.[34] To understand the interaction between chitosan and the solution perovskite precursors, nuclear magnetic resonance (NMR) and Fourier-transform infrared spectroscopy (FTIR) by attenuated total reflectance (ATR) analyses were performed.

The H^1-NMR spectra shown in Figure 1c clearly highlight the interaction in solution between the salified polymer and the perovskite precursors, in particular the FA^+ cation. In the reference spectrum without the polymer, a single signal appears for the two aminic protons of the FA^+ cation, as a result of a rapid interconversion between the two-resonance structure (Figure 1d). Instead, in the presence of the polymer, two distinct signals for the protons a and b are observed. Also, the methine proton of FAI is detected as a singlet at 7.9 ppm in the reference

Figure 1. a) Sketch of the system FAPbI$_3$-salified chitosan in solution. b) Shear viscosity measurement of FAPbI$_3$ + salified chitosan in different amounts. c) NMR spectra of FAPbI$_3$ solution, FAPbI$_3$ + salified chitosan 4 mg mL^{-1}, FAPbI$_3$ + camphorsulfonic acid. d) Representation of the dynamic equilibrium of formamidinium in solution. e) IR spectra of FAPbI$_3$ solution, salified chitosan solution, FAI + salified chitosan 10 mg mL^{-1}, and FAPbI$_3$ + salified chitosan 10 mg mL^{-1}.

spectrum and as a multiplet because of the scalar coupling with the two aminic protons, which are now different. This happens because, whereas in the reference the equilibrium between the resonance structure is allowed by the equal possible distance of the iodide anion from the two –NH$_2$ groups, with the polymer the interconversion is blocked or substantially slowed down.[35] The same effect is observed also when only camphorsulfonic acid is added to the reference, suggesting that it may be the camphorsulfonic group that is responsible for the broken equilibrium which, due to the bigger dimension, cannot be placed at the same distance from the two –NH$_2$ groups, so the shift of the positive charge between the two nitrogen atoms should involve the relocation of the huge group. To further understand the system created in solution, the characteristic vibrational modes are measured by ATR–FTIR analyses (Figure 1e). The IR spectra show a shift of the strong band corresponding to N–H and O–H stretching of the chitosan[36,37] in the region 3435–3379 cm^{-1} for both the solution FAI + polymer and FAPbI$_3$ + polymers, suggesting that the chitosan might interact though hydrogen bonding with the perovskite precursors,[38] in particular with the FA$^+$ cation.

After assessing the nanocomposite solution's properties, the perovskite–polymer films were studied. First, FAPbI$_3$ films were fabricated through spin-coating deposition using antisolvent dripping. Chitosan was added into the perovskite solution in the concentrations of 2 and 4 mg mL^{-1} and the optical and structural properties of the FAPbI$_3$ films with and without polymer were investigated. While the additive does not cause any visible changes in the absorption spectra of the samples (Figure S4a, Supporting Information), notable differences are present in

the X-ray diffraction (XRD) spectra in **Figure 2**a, wherein while the α-phase peak at 13.95°[19,39,40] increases with the amount of chitosan, indicating that the chitosan can positively influence the perovskite crystallization,[41] stabilizing the conductive phase. The peak assigned to the δ-phase at 11.80°[40,42] indeed decreases until it's no longer present when 4 mg mL^{-1} of chitosan is included into the perovskite precursors. The same behavior can be observed for the PbI$_2$ peak at 12.70°,[43] which is present only in the reference sample. This suggests a beneficial effect of the salified chitosan on the stabilization of the α-phase of FAPbI$_3$, as well as promoting the formation of a more crystalline perovskite. The morphologies of the samples are studied through scanning electron microscope (SEM) images which are reported in Figure S5a,b, Supporting Information, and show a superior morphology for the samples containing chitosan, with less grain boundaries and a smoother surface. Moreover, PbI$_2$ is not present, coherently with the XRD pattern, while traces are visible in the FAPbI$_3$ reference. The superior quality of the perovskite–chitosan films is also confirmed by steady-state PL and time-resolved PL analysis. In particular, the PL lifetime spectra shown in Figure 2b show significantly longer average lifetime for the perovskite–chitosan films compared to the reference, confirming the ability of the polymer incorporated in the perovskite to passivate charge traps[44,45] and to boost the formation of higher-quality FAPbI$_3$ films. The lower amount of defect and higher quality of the samples with the chitosan is also confirmed by the higher PL intensities (Figure S4b, Supporting Information). The improved quality of the chitosan-based FAPbI$_3$ films is also observed in the actual solar cell devices.
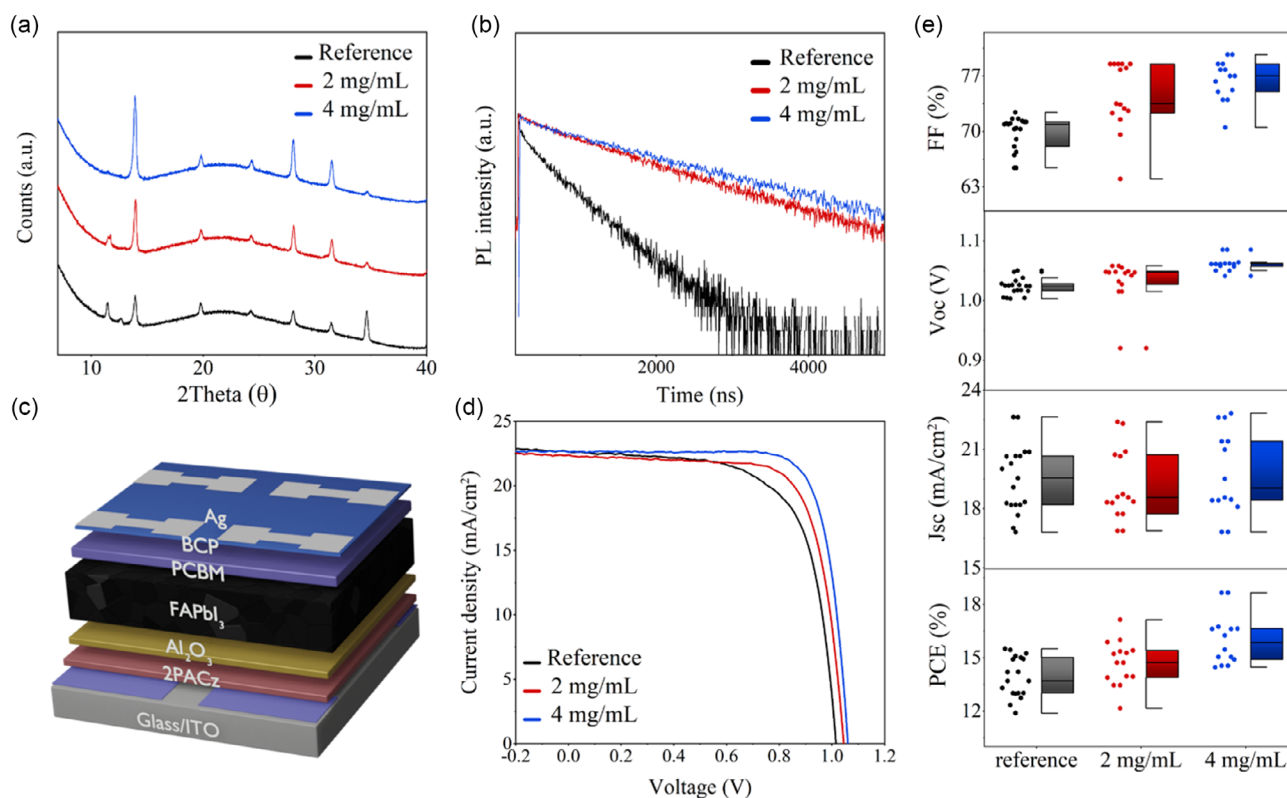
Figure 2. a) XRD patterns of FAPbI$_3$ reference, FAPbI$_3$ + chitosan 2 mg mL^{-1}, and FAPbI$_3$ + chitosan 4 mg mL^{-1}. b) PL lifetime spectra of FAPbI$_3$ reference, FAPbI$_3$ + chitosan 2 mg mL^{-1}, and FAPbI$_3$ + chitosan 4 mg mL^{-1}. c) Sketch of the device's structure. d) Current–voltage curve (I–V) curves. e) Statistical photovoltaic parameters.

The inverted p–i–n configuration devices (indium tin oxide (ITO)/(2-(9H-carbazol-9-yl)ethyl)phosphonic acid (2PACz)[46–48]/Al$_2$O$_3$/FAPbI$_3$/Phenyl-C61-butyric acid methyl ester (PCBM)/Bathocuproine (BCP)/Ag) show an overall increase in performances using the perovskite–chitosan composite, reaching the high efficiency of 18.66% with the 4 mg mL^{-1} composite and confirming the superior optoelectronic quality of the perovskite films made with chitosan. In particular, an increase in the fill factor (FF) and open-circuit voltage (V$_{oc}$) values is observed, suggesting suppressed nonradiative losses in the perovskite-chitosan films,[49] coherently with the observed increase in PL intensity and PL lifetimes (Figure 2d,e).

To elucidate the interaction of chitosan and its salt with the perovskite thin film and explain the reason behind the enhanced performance, DFT calculations were conducted on the prototypical PbI$_2$-terminated surface of FAPbI$_3$ perovskite. All calculations have been carried out at Perdew–Burke–Ernzerhof (PBE)-D3 level, as summarized in the Computational details section. Due to the complexity of the chitosan polymer, it was decided to study its interaction with the perovskite by creating two different "units," as shown in the Figure S6, Supporting Information. The real postsalification system was defined as "full chitosan" and the building blocks as "positive/neutral units" to elucidate the distinct contributions of these interactions on the perovskite surface. The positive unit, where NH$_3^+$ is formed, resulting in a positive charge,

was modeled by placing a Cl$^-$ counterion to maintain the electroneutrality of the system. Using a similar approach, camphorsulfonic acid was modeled by removing H$^+$ from the sulfonic group and introducing a Na$^+$ counterion to maintain charge balance.

Initially, the chemical structure of the salification process forming the system between modified chitosan and camphorsulfonic acid or camphorosulfonate anion was investigated, as depicted in **Figure 3**a,b. The adduct is characterized by a high number of hydrogen bonds, with the protonation of the NH$_2$ group of chitosan significantly stabilizing its formation (Figure 3c).

Table 1 shows the interaction energy between the various proposed systems and the perovskite surface, highlighting the degree of interaction and stabilization. The salified chitosan$^+$/camphorsulfonate$^-$ shows a significant interaction energy, −3.20 eV, indicating a highly stable complex when chitosan is protonated and paired with a camphorosulfate counterion. Similarly, the camphorsulfonate$^-$/Na$^+$ salt shows a strong interaction energy of −3.18 eV, forming a stable complex with the perovskite surface, as shown in **Figure 4**a. The "positive unit" of chitosan salified with Cl$^-$ also shows a significant interaction energy of −3.27 eV, highlighting the crucial role of the protonated NH$_3^+$ group. The "neutral unit" of chitosan shows, instead, a moderate interaction energy of −2.50 eV. These results emphasize the importance of protonation of the chitosan amino group
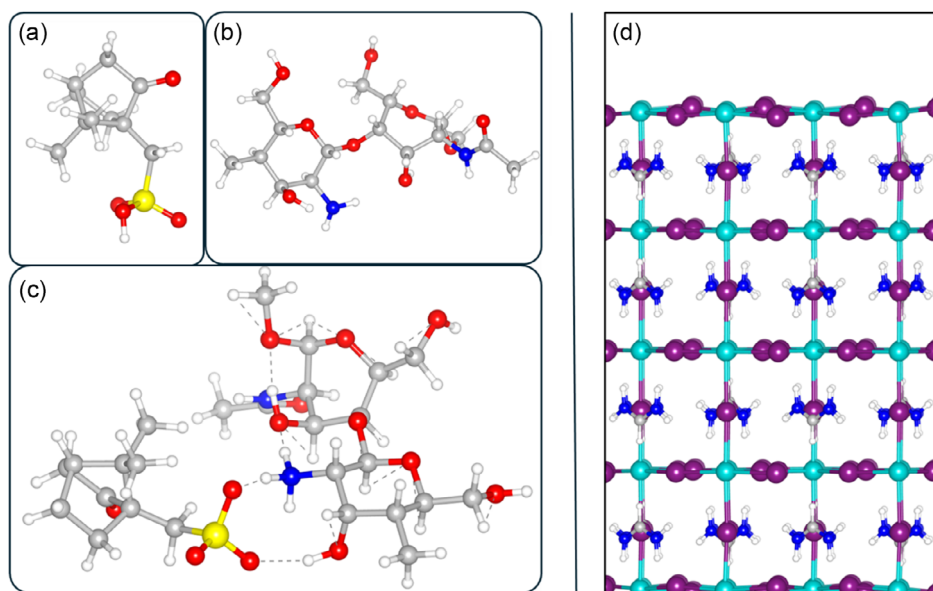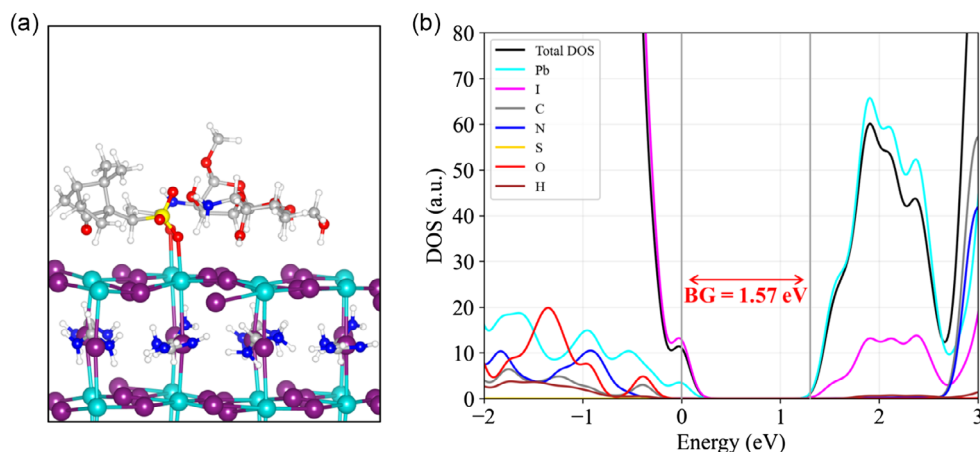
Figure 3. Optimized geometries of a) camphorsulfonic acid, b) chemical-modified chitosan monomer used in this work, c) salified chitosan with camphorsulfonic as conjugated base, d) FAPbI$_3$–PbI$_2$-terminated surface. Color scheme: carbon in gray, oxygen in red, hydrogen in white, sulfur in yellow, lead in cyan, and iodine in purple.

Table 1. Interaction energy of the different systems on the FAPbI$_3$ perovskite exposing the PbI$_2$ terminated surface.

Systems	E_{Ads} [eV]
Chitosan$^+$/camphorsulfonate$^-$	−3.20
Camphorsulfonate$^-$/Na$^+$	−3.18
Chitosan "positive unit"/Cl$^-$	−3.27
Chitosan "neutral unit"	−2.50

and the presence of counterions in enhancing the stability of chitosan and camphorsulfonic acid interactions with the perovskite surface.

As one may notice, the camphorsulfonic anion shows a strong interaction with the perovskite bridging two undercoordinated surface Pb^{2+} ions. This biding motif passivates the surface and introduces no states in the perovskite bandbap, Figure 4b, leading to improved optoelectronic perovskite quality. The interaction between the salified-chitosan and the perovskite in the solid state was also confirmed by FTIR analysis reported in the Figure S7, Supporting Information. In the IR spectrum of the perovskite-CHIC film, a large signal at 3580 cm^{-1} is detected and it can be attributable to O–H and N–H stretching, which is shifted with respect to the signal detectable in the spectrum of the salified chitosan at 3470 cm^{-1}, confirming the interaction in the film. Instead, to better visualize the interaction with the camphorsulfonic group, films of perovskite with sodium


Figure 4. a) Optimized interaction geometry of the salified chitosan with the perovskite surface. b) Partial density of states for the interacting system of (a).

camphorsulfonate (NaCS) were deposited. In the pure NaCS spectrum the asymmetric and symmetric S=O stretching are detected at 1418 and 1204 cm^{-1}, while in the film of perovskite and NaCS the signals are shifted toward lower wavenumbers, indicating an interaction on behalf of the sulfonate group[50] and confirming the theoretical data.

To further exploit the properties of the perovskite–chitosan composite, the solution was deposited with the scalable gravure printing deposition technique, in which the perovskite solution is deposited onto the printing plate with an engraved pattern made of cells with precise engraving parameters which control the volume of solution depending on the depth of the patterns (**Figure 5**a). Finally, the impression roll transfers the solution onto the substrate by applying pressure.[51] Inhomogeneous structures like aggregates and voids are observed when FAPbI$_3$ reference without polymer is deposited without antisolvent baths, which are usually used to control the crystallization process and to obtain a good morphology, despite being a complex and delicate procedure depending on different variables.[52] In this case, when the chitosan is used as an additive, it is possible to avoid the antisolvent bath relying on the salified polymer to control the crystallization process directly, making the deposition more reliable and less complicated. The bonds between the polymer and the perovskite precursors in the solution create a sol–gel system,[53] which causes an increase of viscosity, which actually helps to slow down the otherwise very fast rate of crystallization and allows a single-step full coating of perovskite film with

uniform coverage and defined engraved margins[53,54] where the polymeric additive is positioned between the grain boundaries in the films, protecting and passivating the surface of the perovskite grains[55] (Figure 5b). Moreover, MACl was not used as additive to stabilize the α-phase of FAPbI$_3$ and the photoactive phase was nonetheless stable in the presence of chitosan. To optimize the deposition, chitosan was tested in a range of concentrations between 2 and 10 mg mL^{-1} and the morphologies are compared in Figure 5c. The increased homogeneity in morphology is evident from the SEM images, going from nonuniform morphology in the reference sample, with large aggregates dominating the structure, to an even and uniform morphology in the samples with 2 and 4 mg mL^{-1} of chitosan along with the samples with 8 and 10 mg mL^{-1}, whose morphologies are shown in the Figure S8, Supporting Information. The enhancement in the samples' morphology is also outlined from the atomic force microscopy (AFM) images showing a drastic decrease in the surface roughness from 45 nm for the reference to 10 nm for the highest concentration of chitosan (Figure S9, Supporting Information), allowing a neater interface in the photovoltaic devices. Moreover, the increase of viscosity causes also an increase of the thickness of the perovskite layer, allowing the deposition of a thicker film using the same perovskite concentration (Figure S9f, Supporting Information). The optoelectronic properties of the perovskite–chitosan samples are investigated with PL and PL lifetime spectra, where both identify the samples with 2 and 4 mg mL^{-1} as the optimal ones having both higher PL intensities
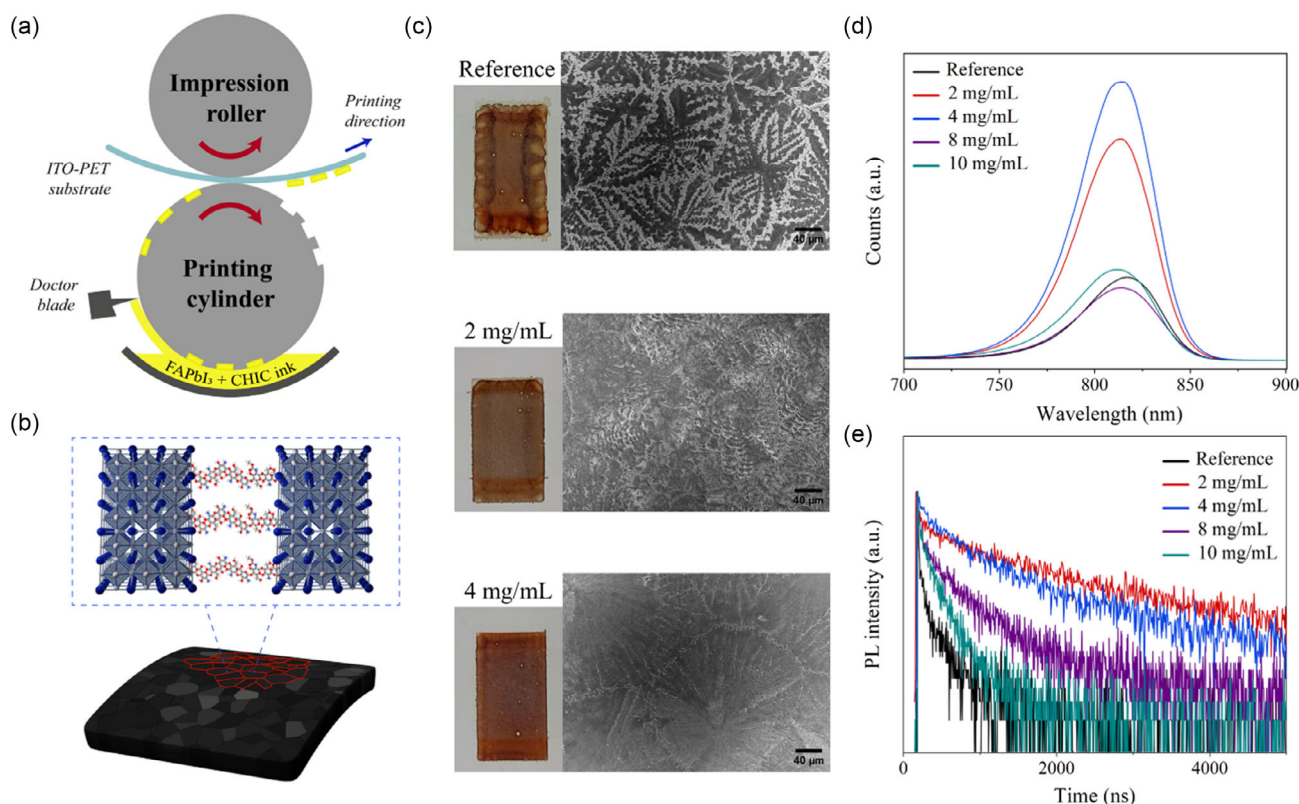
Figure 5. a) Sketch of gravure printing deposition. b) Sketch of the perovskite film with the camphorsulfonic-salified chitosan positioned at the grain boundaries. c) SEM images of gravure-printed samples of FAPbI$_3$ reference, FAPbI$_3$ + chitosan 2 mg mL^{-1}, and FAPbI$_3$ + chitosan 4 mg mL^{-1}. d) PL spectra and e) PL lifetime spectra.

and longer PL lifetimes. The samples with higher concentration of chitosan (8 and 10 mg mL^{-1}) present a drastic decrease in PL intensity and PL lifetimes, although still longer lifetimes compared to the reference sample, hinting at a higher number of defects in the films despite the optimal morphology presented in the SEM images and the lower surface roughness values.

Devices were fabricated with an n–i–p structure on a flexible PET (polyethylene terephthalate) substrate with the following architecture ITO/Tin Oxide (SnO$_2$)/FAPbI$_3$/2,2',7,7'-Tetrakis[N,N-di(4-methoxyphenyl)amino]-9,9'-spirobifluorene (Spiro-OMeTAD)/Au (**Figure 6**). The printing steps of SnO$_2$, FAPbI$_3$, and Spiro-OMeTAD were performed in a controlled atmosphere with 20 °C and relative humidity between 30% and 50% while ITO was sputter coated on the PET and gold as the anode top electrode was thermally evaporated. The photovoltaic performances follow the same trend as the optoelectronic characteristics, showing the highest efficiency for the 2 and 4 mg mL^{-1} chitosan concentrations, achieving respectively 13.4% and 13.1% of PCE. Overall, as a result of the more homogeneous morphology and the defect passivation, the chitosan–perovskite composite shows a substantial increase in the performance, especially in the V_{oc} and J_{sc}, and a summary of the best devices obtained both with spin-coater deposition and gravure printing deposition is reported in **Table 2**, while the average performances are shown in the Table S1, Supporting Information. While the devices differ in architecture, as well as deposition methods, the V_{oc} trend does not change between the two cases, with the 4 mg mL^{-1} concentration having the higher average value, confirming

Table 2. Photovoltaic performances of the best devices based on FAPbI$_3$ reference and FAPbI$_3$ + chitosan fabricated through spin-coater deposition and gravure printing deposition.

	Deposition	FF [%]	V_{oc} [V]	J_{sc} [mA cm^{-2}]	PCE [%]
FAPbI$_3$ ref	Spin coater	67.4	1.02	22.6	15.5
	Gravure printing	58.5	0.92	16.7	8.9
2 mg mL^{-1}	Spin coater	73.4	1.05	22.3	17.1
	Gravure printing	59.4	0.98	23.0	13.4
4 mg mL^{-1}	Spin coater	77.8	1.06	22.6	18.7
	Gravure printing	55.4	1.02	23.1	13.1

the improved quality of the perovskites with fewer defects. Instead, an increase in J_{sc} with the inclusion of the polymer in gravure-printed devices is observed, thanks to the increase in the thickness of the perovskite layer and therefore an increase in the current produced. The main difference can be found in the FF value since in the spin-coater case the 4 mg mL^{-1} has the highest average value, with the 2 mg mL^{-1} very close, while in the rotogravure case the 2 mg mL^{-1} concentration is the highest in average value. The difference here depends on the interfaces between the perovskite layer and transporting layers which are different in the two device architectures. On the other hand, the devices based on the 8 and 10 mg mL^{-1} composites report lower efficiencies, caused mainly by the drastic decrease in current density (J_{sc}), suggesting an insulating effect of the
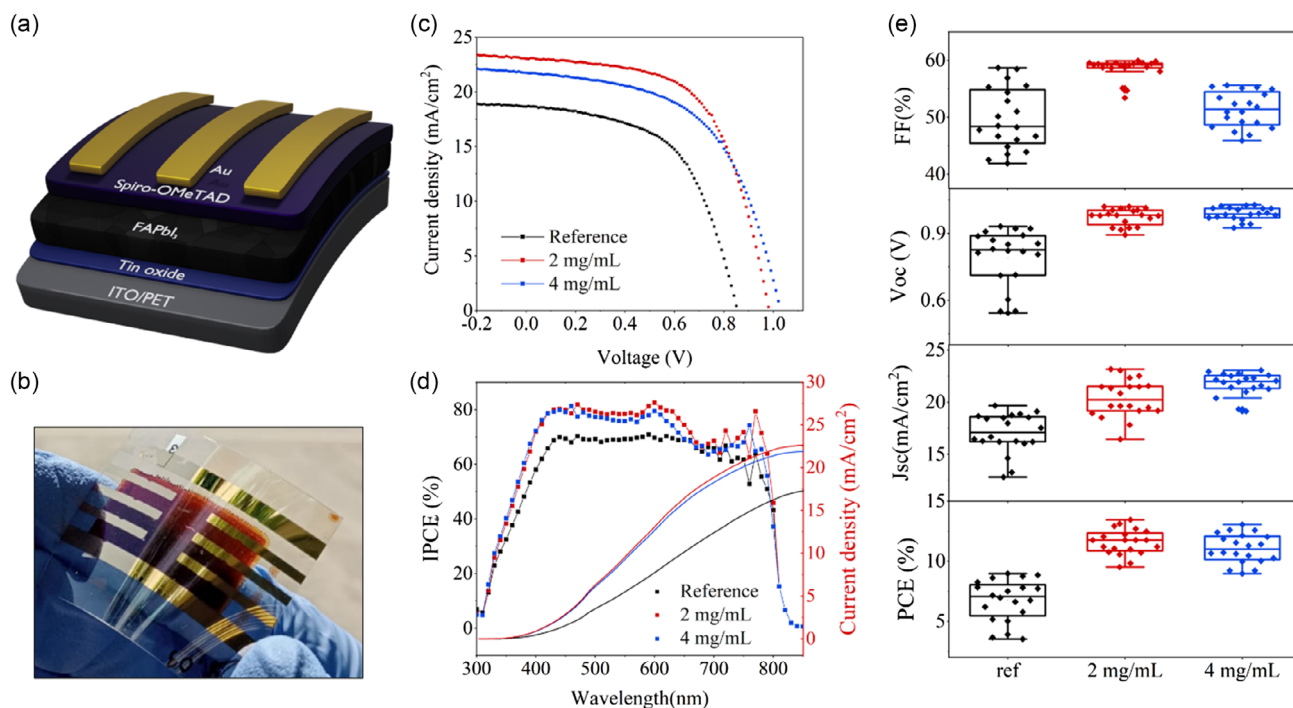

Figure 6. a) Sketch of the device structure. b) Digital photo of gravure printed device. c) I–V curves of FAPbI$_3$ reference, FAPbI$_3$ + chitosan 2 mg mL^{-1}, and FAPbI$_3$ + chitosan 4 mg mL^{-1}. d) Incident photon-to-electron conversion efficiency curves and integrated current density. e) Statistical photovoltaic parameters.

polymer in such concentrations (Figure S10, S11, Supporting Information).

Finally, the stability of the chitosan-perovskite composite was evaluated (**Figure 7**). The air stability of the composite itself was followed by keeping the samples in ambient air for 90 days with relative humidity between 40% and 70% and XRD patterns and absorbance spectra were acquired over time. In all of the XRD patterns in Figure 7a of the pristine samples, small amounts of δ-phase at 11.7° and PbI_2 at 12.6° are detected. However, after the aging in air, the $FAPbI_3$ reference is almost completely transformed into δ-phase, whose peaks notably increased while the α-phase peak decreased. On the other hand, both of the samples with the salified chitosan remain stable over time, maintaining almost the same XRD pattern after aging in air. The absorbance spectra in Figure 7b confirm the observations since the absorption intensity of the $FAPbI_3$ with the chitosan remains stable while the intensity of the reference slowly decreases in

time. The samples with higher amounts of salified chitosan resulted to be even more stable showing only a little presence of δ-phase in the XRD pattern of the $8\,mg\,mL^{-1}$ sample and none in the pattern of the $10\,mg\,mL^{-1}$ sample (Figure S12a, Supporting Information) and no change in the absorbance spectra over time for both (Figure S12b, Supporting Information). Finally, the shelf-life stability of the devices was evaluated both in nitrogen and in ambient air (Figure 7c). Devices based on the 2 and $4\,mg\,mL^{-1}$ composite kept in nitrogen maintained more than 80% of efficiency after 4800 h (Figure S13, Supporting Information), while the reference device degraded under 80% only after 1000 h. The devices were also kept in ambient air without any encapsulation to test the shelf-life stability in air (ISOS-D-1)[56] and while the reference device showed a drastic decrease in efficiency in the 96 h, the 2 and $4\,mg\,mL^{-1}$ composite devices retained more than 80% of the initial efficiency up to 1200 h.
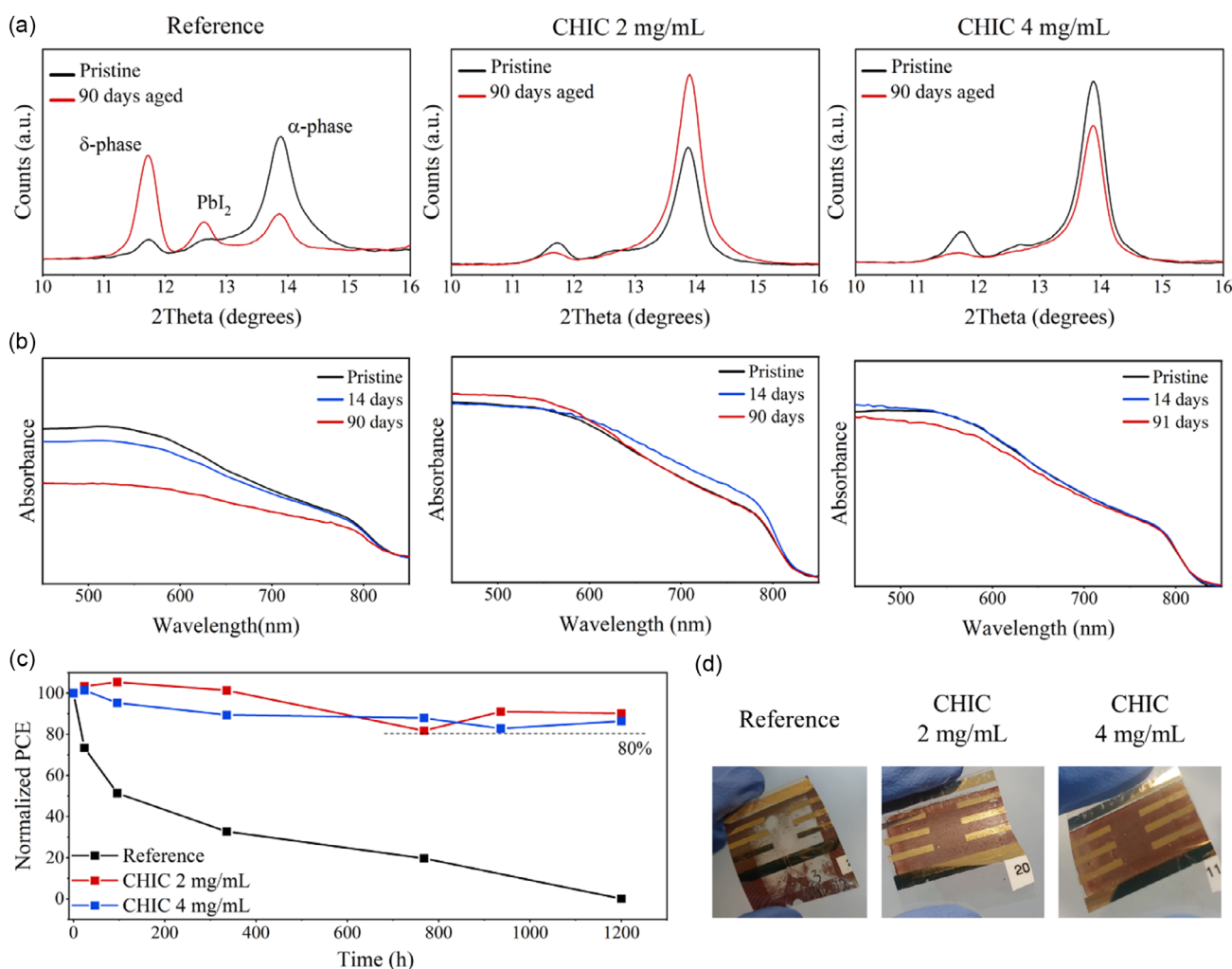
Figure 7. a) XRD patterns of $FAPbI_3$ reference, $FAPbI_3$ + chitosan 2 mg mL^{-1}, and $FAPbI_3$ + chitosan 4 mg mL^{-1} pristine and aged 90 days in ambient air (Relative humidity (RH): 40–70%). b) Absorbance spectra of $FAPbI_3$ reference, $FAPbI_3$ + chitosan 2 mg mL^{-1}, and $FAPbI_3$ + chitosan 4 mg mL^{-1} pristine and aged 90 days in ambient air (RH: 40–70%). c) Shelf-life stability in ambient air of devices based on $FAPbI_3$ reference, $FAPbI_3$ + chitosan 2 mg mL^{-1}, and $FAPbI_3$ + chitosan 4 mg mL^{-1}. d) Digital photos of the devices.

3. Conclusion

In conclusion, a functionalized chitosan was developed to be used as additive for FAPbI$_3$ perovskite deposited first by spin coating and then by gravure printing method. It was seen that if used as a classic additive, the salified chitosan acts as a defect passivator and significantly improves the performances of the p–i–n devices classically fabricated by spin-coating and antisolvent dripping technique. More importantly, when used for the gravure printing method, the additive makes it possible to completely avoid the use of any other crystallization aids involving antisolvent and also any other additive, such as MACl, to stabilize the α-phase of the perovskite thanks to the interactions that the additive establishes with the precursors. Furthermore, due to the modulation of the solution viscosity, the gravure-printed samples with chitosan are homogeneous and with a well-defined pattern. The performances of the corresponding devices are significantly higher compared to the bare perovskite and the shelf life of the devices in air is greatly enhanced. This study provides a general guide to design an effective additive for upscaling the deposition of the perovskite layer and opens the way to trying different combinations of polymers and functional groups. Finally, this straightforward strategy employing a simple additive allows to leave behind difficult techniques and processing such as the antisolvent bath, to look ahead to the upscale of the technology from laboratory scale to larger scale, and ultimately, to industrial application.

4. Experimental Section

Chemicals: Lead (II) iodide (PbI$_2$, ultradry 99.999% metals basis) was purchased from Alfa Aesar (Kandel, Germany); Formamidinium iodide (FAI, >99.99%) and methylammonium chloride (MACl) were from Sigma Aldrich. Chlorobenzene anhydrous, 99.8% (CB); 2-propanol (IPA); bathocuproine, 96% (BCP); aluminum oxide (nanoparticles 20 wt% in water); chitosan (low molecular weight), (+)-camphor-10-sulfonic acid (purum, ≥98.0%); and (+)-camphor-10-sulfonic acid sodium salt (97%) were purchased from Sigma Aldrich. 2PACz [2-(9H-Carbazol-9-yl)ethyl] phosphonic Acid, >98.0%, was purchased from TCI; [6,6]-phenyl C61 butyric acid methyl ester (PCBM) was purchased from Nano-c. Tin (IV) oxide nanoparticles (NPs) (15% in H$_2$O) were purchased from Alfa Aesar, and N2,N2,N20,N20,N7,N7,N70,N70-octakis(4-methoxyphenyl)-9,90-spirobi[9H-fluorene]-2,20,7,70-tetramine (Spiro-MeOTAD), lithium bis(trifluoromethanesulfonyl)imide (R99%, Li-TFSI), 4-tert-butyl pyridine (98%, tBP), and tris(2-(1H-pyrazol-1-yl)-4-tert-butylpyridine) cobalt(III) tri[bis(trifluoromethane) sulfonimide] (FK 209 Co(III) TFSI salt) were purchased from Sigma-Aldrich,

Perovskite Solution Preparation: The FAPbI$_3$ solution for the reference was prepared by dissolving 461 mg of PbI$_2$ (1 mmol), 172 mg of FAI (1 mmol), 13.5 mg of MACl (0.2 mmol) in 1 mL of DMSO and the solution was heated at 80 °C. For the FAPbI$_3$–chitosan solution, the polymer was first dissolved in DMSO at 80 °C for 4 h before adding the perovskite precursors. The FAPbI$_3$–sodium camphorsulfonate was prepared and deposited at the same manner.

Spin-Coater Device Fabrication: The glass ITO patterned substrates (15 × 15 mm²) were sequentially cleaned by ultrasonication in deionized water, acetone, and isopropanol for 10 min each. The ITO substrates were dried with nitrogen and UV–ozone treatment was performed before the hole transport layer deposition. 2PACz (0.5 mg mL^{-1} in ethanol) solution was spin coated in a glove box on ITO substrates at 3000 rpm for 30 s and annealed at 100 °C for 10 min. After cooling them down, the substrates were washed with a solution 0.2 wt% of Al$_2$O$_3$ nanoparticles in ethanol to remove the unbound molecules and then annealed again at 100 °C

for 5 min. The perovskite solution was spin coated in air at 4000 rpm × 20 s and 300 µL of ethyl acetate was dropped on the spinning substrate at 10th second. The substrate was annealed 10 min at 150 °C. 50 nm of the electron transporting layer (ETL) were deposited in glovebox through spin coating of the PCBM solution (25 mg mL^{-1} in chlorobenzene) at 1000 rpm for 60 s. A thin layer of BCP (0.5 mg mL^{-1} in isopropanol) was then deposited by spin coating at 6000 rpm for 20 s. Finally, 80 nm of Ag electrodes were thermally evaporated in high vacuum with an active area of 0.04 cm². The devices were characterized using a Keithley 2400 source measure unit and Air Mass 1.5 Global (AM1.5G) solar simulator (Newport 91160A) exposed to irradiation intensity of 100 (Mw cm^{-2}). The current–voltage curves were acquired in the range from 1.2 to 0.2 V.

Gravure-Printed Device Fabrication: The flexible substrate consisted of ITO-patterned PET(Estman Flexvue OC50) where the ITO pattern was obtained by rotary screen printing of an etching paste (HiEP-300; P & P Solution Co., Ltd). For the printing process, a laboratory-scale gravure printer (Labratester, Norbert Schläfli Maschinen) was used in the fume hood. SnO$_2$ ink was prepared from nanoparticle solution of 15 wt% in water diluted to 2.5 wt% in H$_2$O:IPA 80:20 and it was successively printed with an engraved pattern of 120 lines cm^{-1}, at a speed of 18 m min^{-1}, following annealing in a hot oven at 120 °C for 10 min. The FAPbI$_3$ reference and FAPbI$_3$–chitosan solution were printed using a printing plate with multiple engraved patterns (100, 120, and 140 lines cm^{-1}) at a speed of 18 m min^{-1}, following annealing of the resulting films in a hot oven at 140 °C for 30 min. The Spiro-MeoTAD solution was prepared by mixing 90.9 mg of spiro-MeoTAD in 1 mL of CB and the solution was then doped with 23 µL of Li-TFSI (540 mg mL^{-1} in acetonitrile), 39 µL of tBP, and 10 µL of FK 209 Co(III) TFSI (0.376 mg mL^{-1} in acetonitrile). The spiro-MeOTAD layer was printed with an engraved pattern of 100 lines cm^{-1}, at a speed of 18 m min^{-1}. The devices were completed by thermal evaporation in high vacuum (5.3 10^{-6} mBar) of 100 nm of gold as the anode with a deposition rate of 1 Å s^{-1} and using a mask that defined a 0.09 cm² active area. The J–V curves were acquired using a solar simulator (Newport, Oriel Class A, 91195A) with a voltage source meter (Keithley 2420) under 100 mW cm^{-2} illumination with standard AM1.5G conditions. Light intensity was calibrated by Si reference cell. The J–V measurements were conducted by applying reverse (1.2–0.2 V) and forward (0.2–1.2 V) scan directions with a voltage step of 0.010 V and a scan rate of 0.5 V s^{-1}.

Characterization: The SEM, XRD, absorbance, and PL measurements were conducted as described in a previous report.[20] The AFM images were acquired with the SPM Dimension Icon microscope, from Bruker, using the Peak Force Tapping mode, in air. ^{1}H NMR analyses were performed using a Bruker AVANCE III spectrometer operating at 500 MHz. Temperature was settled at 300 ± 0.1 K. The spin–lattice relaxation time (T1) was measured using the inversion recovery sequence. Transverse proton relaxation time (T2) was measured using the Carr–Purcell–Meiboom–Gill pulse sequence. Three solutions were prepared for NMR analysis. The first solution comprised FAI in DMSO-d6 at a concentration of 10 mM. The second solution was prepared by dissolving both FAI and PbI$_2$ in DMSO-d6, each at a concentration of 10 mM. Each solution underwent stirring for 30 min at room temperature and was subsequently transferred to an NMR tube. The solutions were allowed to equilibrate for 1 h before analysis.

The last solution, containing FAI, PbI$_2$, and CHIC, was prepared by dissolving an appropriate amount of salified chitosan in DMSO-d6 to achieve a concentration of 4 mg mL^{-1}. This solution was stirred at 80 °C for 8 h. After this duration, FAI and PbI$_2$ were added to the chitosan solution to reach a concentration of 10 mM each. The solution underwent stirring for 30 min at room temperature before being transferred to an NMR tube. Once again, the solutions were left to equilibrate for 1 h before analysis. FTIR spectra on the solutions were recorded on 1 M of FAPI solution in DMSO with and without salified chitosan 10 mg mL^{-1} and salified chitosan solubilized in DMSO 10 mg mL^{-1} using a FTIR Jasco 6300 in ATR mode. The FTIR spectra on the films were obtained in diffuse reflectance mode. Each spectrum was acquired with 128 scan and 4 cm^{-1} of resolution. A Malvern Kinexus Pro +, using parallel plate geometry (25 mm radius), was used to investigate the rheological behaviour of the solutions

by varying the chitosan content. The measurements were performed at 23 °C in a shear rate range of 1-1000 s-1.

Computational Details: DFT calculations were carried out on the (001) $FAPbI_3$ surface within the supercell approach using the PBE functional.[57] The plate consisted of a 2×2 tetragonal supercell in the a and b periodic directions and five layers along the perpendicular nonperiodic direction, with a 15 Å region of vacuum added in all cases. Starting from the flat PbI_2 the interaction energy of the different system to the perovskite model was studied. This model and/or the following approach to determine the interaction energy was applied to similar systems and was fully tested in several publications. The total passivation energy (E_{Ads}) was calculated following this equation.

$$E_{Ads} = [E_{pass-slab} - (E_{pristine} - E_{pass})] \tag{1}$$

where $E_{pass-slab}$ is the total energy of the passivated slab; $E_{pristine}$ is the total energy of the pristine PbI_2-terminated bare surface; and E_{pass} is the energy of the isolated molecule. Dispersion interactions were considered on the optimized geometries using the D3 approach of Grimme.[58] The isolated molecule geometries were optimized using 20 Å supercells, which were large enough to decouple long-range interactions. All calculations using Quantum Espresso software[59] using ultrasoft pseudopotentials with a cutoff on the wavefunction of 40 and 320 Ryd for the grid and using Gamma-centered grids in the Brillouin zone.

Supporting Information

Supporting Information is available from the Wiley Online Library or from the author.

Acknowledgements

Conflict of Interest

P.B. and R.P. are employees at Eni S.p.A, a company involved in perovskite photovoltaics R&D. A patent application has been filed with the Italian Patent Office, covering the work presented in this article.

Author Contributions

Nadir Vanni: Data curation (lead); Formal analysis (lead); Investigation (lead); Methodology (lead); Writing—original draft (lead). **Antonella Giuri**: Conceptualization (equal); Formal analysis (supporting); Supervision (supporting); Writing—review & editing (equal). **Mario Calora**: Data curation (supporting); Methodology (supporting); Writing—review & editing (supporting). **Edoardo Podda**: Investigation (supporting); Methodology (supporting); Writing—review & editing (supporting). **Anna Paola Caricato**: Funding acquisition (supporting); Supervision (supporting); Writing—review & editing (supporting). **Katia Sparnacci**: Conceptualization (supporting); Formal analysis (supporting); Supervision (equal); Writing—review & editing (supporting). **Riikka Suhonen**: Data curation (supporting); Methodology (equal); Supervision (equal); Writing—review & editing (supporting). **Mari Ylikunnari**: Supervision (supporting); Writing—review & editing (supporting). **Amanda Covarelli**: Data curation (supporting); Formal analysis (equal); Methodology (equal); Writing—original draft (equal). **Luca Gregori**: Data curation (supporting); Formal analysis (supporting); Writing—review & editing (supporting). **Filippo De Angelis**: Formal analysis (equal); Funding acquisition (equal); Supervision (equal); Writing—review & editing (equal). **Gianluigi Marra**: Data curation (supporting); Formal analysis (supporting); Writing—review & editing (supporting). **Paolo Biagini**: Conceptualization (equal); Funding acquisition (equal); Supervision (supporting); Writing—review & editing (supporting). **Riccardo Po'**: Conceptualization (equal); Funding acquisition (equal); Supervision (supporting); Writing—review & editing (supporting). **Aurora Rizzo**: Conceptualization (lead); Data curation (lead); Funding acquisition (lead); Supervision (lead); Writing—review & editing (lead).

Data Availability Statement

The data that support the findings of this study are available from the corresponding author upon reasonable request.

[1] Q. Wang, N. Phung, D. Di Girolamo, P. Vivo, A. Abate, *Energy Environ. Sci.* **2019**, *12*, 865.
[2] A. Sadhanala, S. Ahmad, B. Zhao, N. Giesbrecht, P. M. Pearce, F. Deschler, R. L. Z. Hoye, K. C. Gödel, T. Bein, P. Docampo, S. E. Dutton, M. F. L. De Volder, R. H. Friend, *Nano Lett.* **2015**, *15*, 6095.
[3] C. Wehrenfennig, G. E. Eperon, M. B. Johnston, H. J. Snaith, L. M. Herz, *Adv. Mater.* **2014**, *26*, 1584.
[4] H. J. Snaith, *J. Phys. Chem. Lett.* **2013**, *4*, 3623.
[5] J. Y. Kim, J.-W. Lee, H. S. Jung, H. Shin, N.-G. Park, *Chem. Rev.* **2020**, *120*, 7867.
[6] N. Li, X. Niu, Q. Chen, H. Zhou, *Chem. Soc. Rev.* **2020**, *49*, 8235.
[7] P. Roy, N. Kumar Sinha, S. Tiwari, A. Khare, *Sol. Energy* **2020**, *198*, 665.
[8] S. Masi, A. Rizzo, R. Munir, A. Listorti, A. Giuri, C. Esposito Corcione, N. D. Treat, G. Gigli, A. Amassian, N. Stingelin, S. Colella, *Adv. Energy Mater.* **2017**, *7*, 1602600.

[9] K. Yan, M. Long, T. Zhang, Z. Wei, H. Chen, S. Yang, J. Xu, *J. Am. Chem. Soc.* **2015**, *137*, 4460.

[10] I. Mesquita, L. Andrade, A. Mendes, *Sol. Energy* **2020**, *199*, 474.

[11] Y. Xie, Q. Xue, H. Yip, *Adv. Energy Mater.* **2021**, *11*, 2100784.

[12] M. Konstantakou, D. Perganti, P. Falaras, T. Stergiopoulos, *Crystals* **2017**, *7*, 291.

[13] G. Jang, H. Kwon, S. Ma, S. Yun, H. Yang, J. Moon, *Adv. Energy Mater.* **2019**, *9*, 1901719.

[14] G. Tang, F. Yan, *J. Semicond.* **2021**, *42*, 101606.

[15] C. Zuo, D. Vak, D. Angmo, L. Ding, M. Gao, *Nano Energy* **2018**, *46*, 185.

[16] H. Min, M. Kim, S.-U. Lee, H. Kim, G. Kim, K. Choi, J. H. Lee, S. I. Seok, *Science* **2019**, *366*, 749.

[17] J. Park, J. Kim, H.-S. Yun, M. J. Paik, E. Noh, H. J. Mun, M. G. Kim, T. J. Shin, S. I. Seok, *Nature* **2023**, *616*, 724.

[18] V. L. Pool, B. Dou, D. G. Van Campen, T. R. Klein-Stockert, F. S. Barnes, S. E. Shaheen, M. I. Ahmad, M. F. A. M. Van Hest, M. F. Toney, *Nat. Commun.* **2017**, *8*, 14075.

[19] T. Liu, Y. Zong, Y. Zhou, M. Yang, Z. Li, O. S. Game, K. Zhu, R. Zhu, Q. Gong, N. P. Padture, *Chem. Mater.* **2017**, *29*, 3246.

[20] K. M. M. Salim, S. Masi, A. F. Gualdrón-Reyes, R. S. Sánchez, E. M. Barea, M. Kreĉmarová, J. F. Sánchez-Royo, I. Mora-Seró, *ACS Energy Lett.* **2021**, *6*, 3511.

[21] N. Vanni, R. Pò, P. Biagini, G. Bravetti, S. Carallo, A. Giuri, A. Rizzo, *Nanomaterials* **2024**, *14*, 107.

[22] J. Jeong, M. Kim, J. Seo, H. Lu, P. Ahlawat, A. Mishra, Y. Yang, M. A. Hope, F. T. Eickemeyer, M. Kim, Y. J. Yoon, I. W. Choi, B. P. Darwich, S. J. Choi, Y. Jo, J. H. Lee, B. Walker, S. M. Zakeeruddin, L. Emsley, U. Rothlisberger, A. Hagfeldt, D. S. Kim, M. Grätzel, J. Y. Kim, *Nature* **2021**, *592*, 381.

[23] Z. Huang, M. Wei, A. H. Proppe, H. Chen, B. Chen, Y. Hou, Z. Ning, E. Sargent, *Adv. Funct. Mater.* **2021**, *31*, 2010572.

[24] L. Bi, Q. Fu, Z. Zeng, Y. Wang, F. R. Lin, Y. Cheng, H.-L. Yip, S. W. Tsang, A. K.-Y. Jen, *J. Am. Chem. Soc.* **2023**, *145*, 5920.

[25] M. Kim, G.-H. Kim, T. K. Lee, I. W. Choi, H. W. Choi, Y. Jo, Y. J. Yoon, J. W. Kim, J. Lee, D. Huh, H. Lee, S. K. Kwak, J. Y. Kim, D. S. Kim, *Joule* **2019**, *3*, 2179.

[26] S. R. Raga, M.-C. Jung, M. V. Lee, M. R. Leyden, Y. Kato, Y. Qi, *Chem. Mater.* **2015**, *27*, 1597.

[27] D.-H. Kang, S.-U. Lee, N.-G. Park, *ACS Energy Lett.* **2023**, *8*, 2122.

[28] L. Chen, M. Hu, S. Lee, J. Kim, Z.-Y. Zhao, S.-P. Han, M. S. Lah, S. I. Seok, *J. Am. Chem. Soc.* **2023**, *145*, 27900.

[29] G. Bravetti, N. Taurisano, A. Moliterni, J. M. Vicent-Luna, D. Altamura, F. Aiello, N. Vanni, A.-L. Capodilupo, S. Carallo, G. Gigli, G. Uccello-Barretta, F. Balzano, C. Giannini, S. Tao, S. Colella, A. Rizzo, *Chem. Mater.* **2024**, *36*, 3150.

[30] R. Chen, Y. Wang, S. Nie, H. Shen, Y. Hui, J. Peng, B. Wu, J. Yin, J. Li, N. Zheng, *J. Am. Chem. Soc.* **2021**, *143*, 10624.

[31] Z. Guo, T. Gao, J. Zhuang, X. Liu, H. Guo, J. Yi, Z. Ma, H. Li, X. Cheng, *ACS Appl. Energy Mater.* **2021**, *4*, 4910.

[32] Y. Zou, R. Guo, A. Buyruk, W. Chen, T. Xiao, S. Yin, X. Jiang, L. P. Kreuzer, C. Mu, T. Ameri, M. Schwartzkopf, S. V. Roth, P. Müller-Buschbaum, *ACS Appl. Mater. Interfaces* **2020**, *12*, 52643.

[33] R. Vidal, J.-A. Alberola-Borràs, S. N. Habisreutinger, J.-L. Gimeno-Molina, D. T. Moore, T. H. Schloemer, I. Mora-Seró, J. J. Berry, J. M. Luther, *Nat. Sustainable* **2021**, *4*, 277.

[34] F. Bisconti, A. Giuri, L. Dominici, S. Carallo, E. Quadrivi, R. Po', P. Biagini, A. Listorti, C. E. Corcione, S. Colella, A. Rizzo, *Nano Energy* **2021**, *89*, 106406.

[35] N. Vanni, A. Giuri, G. Bravetti, R. Marrazzo, E. Quadrivi, C. Marchini, S. Spera, M. R. Guascito, R. Pò, P. Biagini, A. Rizzo, *ACS Appl. Mater. Interfaces* **2024**, *16*, 40927.

[36] M. Fernandes Queiroz, K. Melo, D. Sabry, G. Sassaki, H. Rocha, *Mar. Drugs* **2015**, *13*, 141.

[37] C. Branca, G. D'angelo, C. Crupi, K. Khouzami, S. Rifici, G. Ruello, U. Wanderlingh, *Polymer* **2016**, *99*, 614.

[38] A. Giuri, S. Masi, A. Listorti, G. Gigli, S. Colella, C. Esposito Corcione, A. Rizzo, *Nano Energy* **2018**, *54*, 400.

[39] M. T. Weller, O. J. Weber, J. M. Frost, A. Walsh, *J. Phys. Chem. Lett.* **2015**, *6*, 3209.

[40] T. A. S. Doherty, S. Nagane, D. J. Kubicki, Y.-K. Jung, D. N. Johnstone, A. N. Iqbal, D. Guo, K. Frohna, M. Danaie, E. M. Tennyson, S. Macpherson, A. Abfalterer, M. Anaya, Y.-H. Chiang, P. Crout, F. S. Ruggeri, S. Collins, C. P. Grey, A. Walsh, P. A. Midgley, S. D. Stranks, *Science* **2021**, *374*, 1598.

[41] Y. Niu, D. He, Z. Zhang, J. Zhu, T. Gavin, P. Falaras, L. Hu, *J. Energy Chem.* **2022**, *68*, 12.

[42] M. R. A. Elsayed, A. M. Elseman, A. A. Abdelmageed, H. M. Hashem, A. Hassen, *Sci. Rep.* **2023**, *13*, 10115.

[43] G. Wang, L. Wang, J. Qiu, Z. Yan, K. Tai, W. Yu, X. Jiang, *Sol. Energy* **2019**, *187*, 147.

[44] Y. Yamada, T. Nakamura, M. Endo, A. Wakamiya, Y. Kanemitsu, *J. Am. Chem. Soc.* **2014**, *136*, 11610.

[45] D. W. De Quilettes, S. M. Vorpahl, S. D. Stranks, H. Nagaoka, G. E. Eperon, M. E. Ziffer, H. J. Snaith, D. S. Ginger, *Science* **2015**, *348*, 683.

[46] X. Liu, B. Li, M. Han, X. Zhang, J. Chen, S. Dai, *Acta Chim. Sin.* **2024**, *82*, 348.

[47] M. Li, M. Liu, F. Qi, F. R. Lin, A. K.-Y. Jen, *Chem. Rev.* **2024**, *124*, 2138.

[48] X. Zhang, S. Zhang, X. Liao, B. Ding, G. Rahim, K. Zhao, J. Chen, M. Han, Y. Zhou, P. Shi, K. Zhang, S. Kinge, H. Zhang, R. Wang, K. G. Brooks, S. Dai, X. Liu, Z. Fei, P. J. Dyson, M. K. Nazeeruddin, Y. Ding, *Adv. Funct. Mater.* **2024**, *34*, 2314086.

[49] M. Degani, Q. An, M. Albaladejo-Siguan, Y. J. Hofstetter, C. Cho, F. Paulus, G. Grancini, Y. Vaynzof, *Sci. Adv.* **2021**, *7*, 49.

[50] Q. Cao, Y. Li, H. Zhang, J. Yang, *Sci. Adv.* **2021**, *7*, 28.

[51] Y. Y. Kim, T. Yang, R. Suhonen, M. Välimäki, T. Maaninen, A. Kemppainen, N. J. Jeon, J. Seo, *Adv. Sci.* **2019**, *6*, 1802094.

[52] Y. Y. Kim, T.-Y. Yang, R. Suhonen, A. Kemppainen, K. Hwang, N. J. Jeon, J. Seo, *Nat. Commun.* **2020**, *11*, 5146.

[53] A. Giuri, N. Vanni, M. Ahmad, N. Rolston, C. Esposito Corcione, A. Listorti, S. Colella, A. Rizzo, *Mater. Adv.* **2023**, *4*, 4294.

[54] F. Bisconti, A. Giuri, R. Suhonen, T. M. Kraft, M. Ylikunnari, V. Holappa, R. Po', P. Biagini, A. Savoini, G. Marra, S. Colella, A. Rizzo, *Cell Rep. Phys. Sci.* **2021**, *2*, 100639.

[55] F. Bisconti, M. Leoncini, S. Gambino, N. Vanni, S. Carallo, F. Russo, V. Armenise, A. Listorti, S. Colella, S. Valastro, A. Alberti, G. Mannino, A. Rizzo, *ACS Nano* **2024**, *18*, 1573.

[56] M. V. Khenkin, E. A. Katz, A. Abate, G. Bardizza, J. J. Berry, C. Brabec, F. Brunetti, V. Bulović, Q. Burlingame, A. Di Carlo, R. Cheacharoen, Y.-B. Cheng, A. Colsmann, S. Cros, K. Domanski, M. Dusza, C. J. Fell, S. R. Forrest, Y. Galagan, D. Di Girolamo, M. Grätzel, A. Hagfeldt, E. Von Hauff, H. Hoppe, J. Kettle, H. Köbler, M. S. Leite, S. Liu, Y.-L. Loo, J. M. Luther, et al. *Nat. Energy* **2020**, *5*, 35.

[57] J. P. Perdew, K. Burke, M. Ernzerhof, *Phys. Rev. Lett.* **1996**, *77*, 3865.

[58] S. Grimme, J. Antony, S. Ehrlich, H. Krieg, *J. Chem. Phys.* **2010**, *132*, 154104.

[59] P. Giannozzi, O. Andreussi, T. Brumme, O. Bunau, M. Buongiorno Nardelli, M. , R. Car, C. Cavazzoni, D. Ceresoli, M. Cococcioni, N. Colonna, I. Carnimeo, A. Dal Corso, S. De Gironcoli, P. Delugas, R. A. Distasio, A. Ferretti, A. Floris, G. Fratesi, G. Fugallo, R. Gebauer, U. Gerstmann, F. Giustino, T. Gorni, J. Jia, M. Kawamura, H.-Y. Ko, A. Kokalj, E. Küçükbenli, M. Lazzeri, et al. *J. Phys. Condens. Matter.* **2017**, *29*, 465901.

2400612 (11 of 11)